Reynolds stress closure modeling in wall-bounded flows

By P. A. Durbin

This report describes two projects. Firstly, a Reynolds stress closure for near-wall turbulence is described. It was motivated by the simpler $k-\varepsilon-\overline{v^2}$ model described in last year's annual research brief.

DNS of three-dimensional channel flow show a curious decrease of the turbulent kinetic energy. The second topic of this report is a model which reproduces this effect. That model is described and used to discuss the relevance of the three-dimensional channel flow simulation to swept wing boundary layers.

1. Motivation and objectives

The region of a flow very near to a surface exerts a disproportionate control on transport of momentum and heat between surface and fluid. The turbulence in this region is strongly inhomogeneous and highly anisotropic. The anisotropy is particularly important: the normal component of turbulent intensity ($\overline{v^2}$) is responsible for transport to and from the surface; this component is suppressed by the proximate surface. The behavior of $\overline{v^2}$ was the focus of attention in our previous work on near-wall modeling (Durbin 1991). An elliptic relaxation equation was formulated to describe the suppression of $\overline{v^2}$ and to allow appropriate boundary conditions to be satisfied. Last year's report described an application of the $k-\varepsilon-\overline{v^2}$ model to boundary layers and heat transfer.

During the period covered by the present report the near-wall formulation was extended to a full Reynolds stress closure. This formulation is tensorally invariant: $\overline{v^2}$ is not singled out as the normal component; the full Reynolds stress model is applicable to general geometries. The application of this model to separated flows is described in the article by S. Ko in the present volume. The model and an assessment of its predictive potential are described in section 2.1.

Moin *et al.* (1990) performed a DNS of three-dimensional channel flow in order to provide detailed data for use in modeling. This flow was meant as an idealization of the swept-wing boundary layer. We have attempted to model three-dimensional channel flow and to assess the relevance of this flow to the infinite swept wing boundary layer. The most peculiar feature observed in the DNS was a *decrease* of the turbulent intensity when the cross-stream pressure gradient was applied. One would expect the cross-stream flow to add a new contribution to turbulence production and to *increase* the turbulence intensity; indeed, this is what existing turbulence models predict. To account for the reduction in intensity, we have assumed that the streamwise vorticity produced by the cross-flow enhances the cascade of energy to small scales. The mechanism might involve breakup of large, streamwise eddies. The present model consists simply of a parameterization of

three-dimensionality and an *ad hoc* modification to the ε-equation. With only this modification, the Reynolds stress model reproduces many of the features observed in the DNS. Three-dimensional shear flow is discussed in section 2.2.

2. Accomplishments

2.1 The Reynolds stress model

A detailed description of the Reynolds stress model is provided in Durbin (1992a); the following is a brief summary.

The exact Reynolds stress transport equation can be written

$$D_t\overline{u_iu_j} = \wp_{ij} + P_{ij} - \frac{\overline{u_iu_j}}{k}\varepsilon - \partial_k\overline{u_ku_iu_j} + \nu\nabla^2\overline{u_iu_j} \tag{1}$$

where $D_t(\bullet)$ is the convective derivative following the mean flow;

$$P_{ij} = -\overline{u_iu_k}\partial_kU_j - \overline{u_ju_k}\partial_kU_i \tag{2}$$

is the rate of turbulence production by mean velocity gradients, and

$$\wp_{ij} = -\frac{1}{\rho}\overline{u_i\partial_jp} - \frac{1}{\rho}\overline{u_j\partial_ip} - \varepsilon_{ij} + \frac{\overline{u_iu_j}}{k}\varepsilon \tag{3}$$

is the redistribution tensor. (The trace of (3) is not equal to zero, but it is common practice to ignore the trace of $\wp_{ij}$ on the grounds either that it is negligible or that it is a 'pressure diffusion' term that can be absorbed in the self-transport model.) The Rotta model for anisotropic dissipation, $-\overline{u_iu_j}\varepsilon/k$, has been added to (1) and subtracted from (3): among other virtues, this has the effect of making $\wp_{ij}$ vanish at rigid, no-slip boundaries. By definition, $\varepsilon = \varepsilon_{ii}/2$ is the rate of dissipation of turbulent kinetic energy (k).

In the notation of equation (3), all unclosed terms have been incorporated into $\wp_{ij}$ except for the transport terms. We follow the usual practice of modeling turbulent self- transport by gradient diffusion:

$$-\partial_l\overline{u_lu_iu_j} = \partial_l\left(\frac{\nu_{T_{lm}}}{\sigma_k}\partial_m\overline{u_iu_j}\right). \tag{4}$$

This amounts to regarding u_iu_j as a 'substance' being transported by the turbulent velocity u_l. The diffusional model is as much a representation of the smoothing effect of ensemble averaging as of convective transport *per se*: this is why the model is parabolic rather than hyperbolic. For the eddy viscosity,

$$\nu_{T_{ij}} = C_\mu\overline{u_iu_j}\,T \tag{5}$$

will be used. For the time scale T, we adopt

$$T = \max\left(\frac{k}{\varepsilon},\ C_T\left(\frac{\nu}{\varepsilon}\right)^{1/2}\right). \tag{6}$$

This becomes k/ε far from boundaries. Near a surface where $k \to 0$, it becomes the Kolmogorov time-scale $C_T(\nu/\varepsilon)^{1/2}$, which is a suitable lower bound on T.

A second order closure for $\wp_{ij}$ is simply a proposed relationship between this unknown and the dependent variable of equation (1), $\overline{u_i u_j}$. In all closures to date, this relationship has consisted of algebraic formulae. However, those formulae are based on quasi-homogeneous assumptions—most notably in the rapid pressure strain term—which are incorrect in the strongly inhomogeneous near wall region. I have proposed in previous reports that elliptic effects within the flow that are caused by the proximity of a boundary might be included by formulating an elliptic relaxation model for $\wp_{ij}$. Because the exact elliptic effects are inherently non-local, they cannot appear explicitly in a *single* point model; they are represented quite indirectly by the present model.

The elliptic relaxation model can be put into coordinate independent form and written

$$\wp_{ij} = k f_{ij} \tag{7}$$

$$L^2 \nabla^2 f_{ij} - f_{ij} = -\Pi_{ij}. \tag{8}$$

The length scale L is formulated by analogy to (6):

$$L = C_L \max\left(\frac{k^{3/2}}{\varepsilon}, C_\eta \left(\frac{\nu^3}{\varepsilon}\right)^{1/4}\right). \tag{9}$$

Boundary conditions influence the solution in the interior of the flow through the homogeneous solutions to (8) (Durbin 1992a). Far from the surface, these solutions decay, and the f_{ij} relax to quasi-homogeneity, as represented by a balance of the second term on the left side of (8) with its right side.

Any quasi-homogeneous model can be used for Π_{ij}. Here we adopt the simple model recommended by Launder (1989). This consists of a sum of Rotta's return to-isotropy and the isotropization-of-production models:

$$\Pi_{ij} = \frac{1 - C_1}{kT}\left(\overline{u_i u_j} - \frac{2}{3}k\delta_{ij}\right) - \frac{C_2}{k}\left(P_{ij} - \frac{2}{3}P\delta_{ij}\right) \tag{10}$$

where $2P = P_{ii}$, and P_{ij} is given by (2). C_1 is the usual Rotta constant, and $C_2 = 3/5$ is found by the method of perturbation of isotropy.

2.1.1 Assessment of the model

The viability of the present Reynolds stress closure was assessed by computing various boundary layer flows. An initial, detailed evaluation of the approach consisted of comparing the model solution to DNS data on channel flow; this comparison is provided in Figure 1. The near wall behavior of the components of the Reynolds stress tensor is captured very well by the model.

Durbin (1992a) contains further comparisons to data in zero pressure gradient, adverse pressure gradient, and curved wall boundary layers. I will not repeat all of those comparisons here, but simply provide a few representative figures. I will

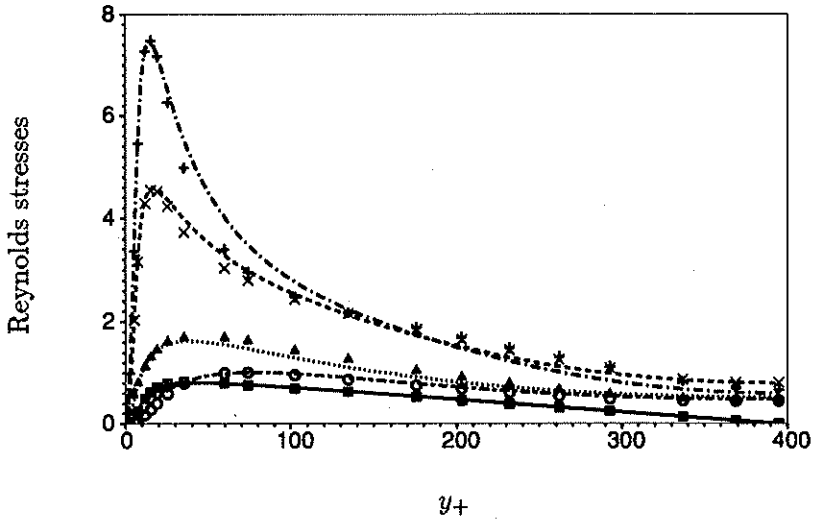

FIGURE 1. Comparison of model (lines) to DNS (symbols) profiles of Reynolds stresses in channel flow at $R_\tau = 395$. +, $\overline{u^2}$; ×, k; △, $\overline{w^2}$; ○, $\overline{v^2}$; ■, $-\overline{uv}$.

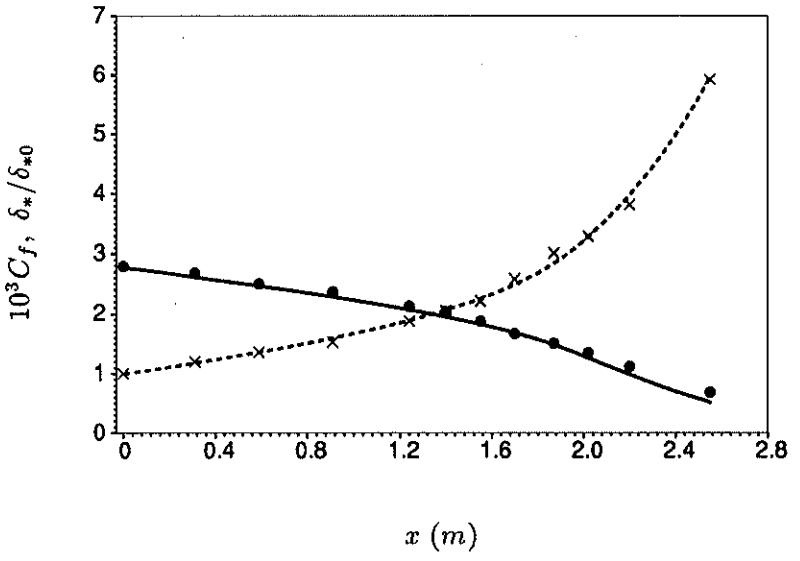

FIGURE 2. Friction coefficient (•) and displacement thickness (×) versus downstream distance for the Samuel and Joubert experiment. Curves are solution of model, symbols experimental data.

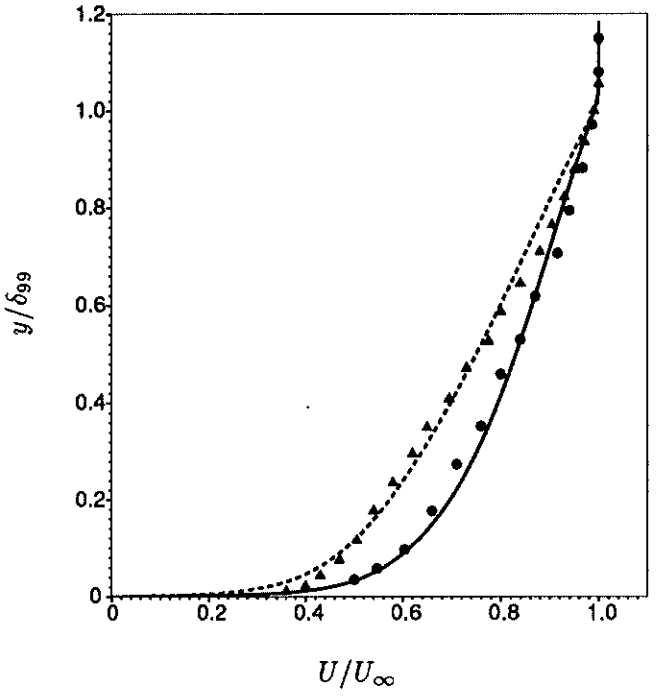

FIGURE 3. Mean velocity profiles at stations 9 ($x = 1.87\,m$, •) and 12 ($x = 2.55\,m$, △) of the Samuel and Joubert adverse pressure gradient boundary layer. Lines are model, symbols experiment.

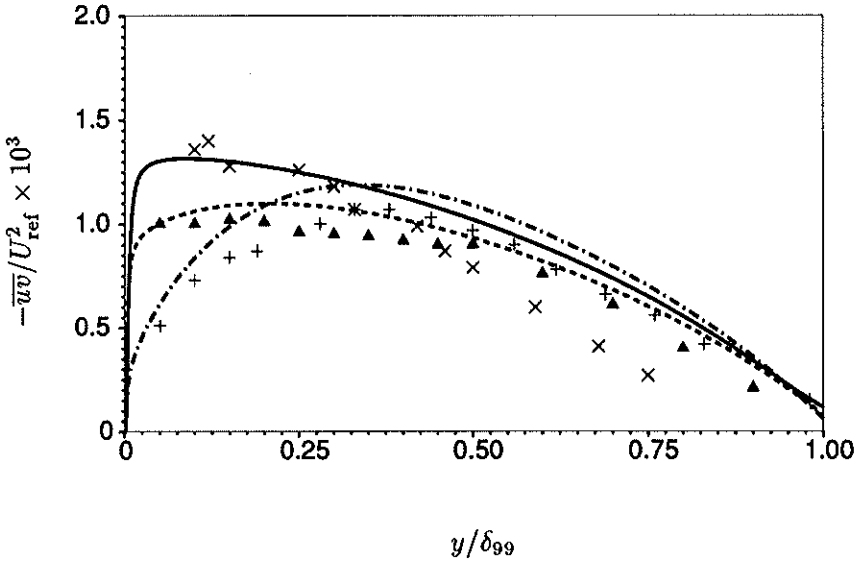

FIGURE 4. Reynolds shear stress profiles at stations T1 ($x = 0.19\,m$, ×, ——), T4 ($x = 1.53\,m$, △, - - -) and T6 ($x = 2.54\,m$, +, —·—) of Samuel and Joubert (1974). Curves are model, symbols experimental data.

skip the zero pressure gradient case. It provides a necessary prerequisite for any near wall turbulence model. The present model gives an excellent solution for the dependence of skin friction on Reynolds number and quite satisfactory profiles of mean velocity and turbulent Reynolds stresses.

The Samuel and Joubert (1974) experiment on a boundary layer progressing into a region of increasingly adverse pressure gradient is a good test of the response of a model to pressure gradients. Solutions for skin friction and displacement thickness versus downstream distance are shown in Figure 2 along with experimental data. Profiles of mean velocity and Reynolds shear stress are contained in figures 3 and 4. Agreement between the model and data is quite reasonable, although discrepancies clearly can be seen. It is encouraging that the model is able to describe the departure from equilibrium observed in the experiment; in particular, Figure 4 shows how the pressure gradient causes a change of the near wall region from a constant stress layer to a layer of increasing stress. The log-layer theory invokes a constant stress layer.

A nice illustration of the capability of the Reynolds stress model is provided by the boundary layer on a convex curved surface. A tensorially consistent model is formally independent of coordinate system. This means that the model equations can be projected onto curvilinear coordinates by the methods of differential geometry. Upon doing so, metric terms arise. The stabilizing effect of convex curvature can be attributed to those metric terms. Thus, much of the important physics are retained by the coordinate invariant Reynolds stress model. By contrast, noninvariant models (*e. g.,* mixing length) can not account for curvature effects, nor can quasi-isotropic, scalar models (*e. g.,* $k - \varepsilon$).

Figure 5 shows the downstream evolution of the skin friction coefficient in a boundary layer that starts on a flat plate, then flows around a 90° convex, circular arc, and then continues along another flat section. This boundary layer was studied experimentally by Simon *et al.* (1982). In the experiment, the wind tunnel wall opposite to the test surface was contoured to maintain a constant surface pressure beneath the boundary layer. A pressure gradient normal to the curved wall exists to balance the centrifugal acceleration.

The dashed line in Figure 5 shows the downstream evolution of C_f on a flat plate. Convex curvature begins at $x = 0$; the skin friction drops abruptly. In Figure 5, C_f has been normalized by its value at the start of curvature. This normalization enables one to invoke Reynolds analogy and include data on heat transfer coefficients in the figure. The heat transfer data are more comprehensive than the skin friction data and they were measured directly; the skin friction had to be inferred by assuming that the mean velocity profiles conformed to the universal, constant stress log-law.

In fact, in the curved section the Reynolds shear stress profile does not show a constant stress layer near the surface. Figure 6 shows how the centrifugal stabilization suppresses $-\overline{uv}$ in the outer region of the boundary layer. Indeed, $-\overline{uv}$ becomes slightly negative in the data denoted by $\times$ when $y/\delta_{99} > 0.4$. After the curved section, $-\overline{uv}$ initially recovers near the surface, and the region of increased

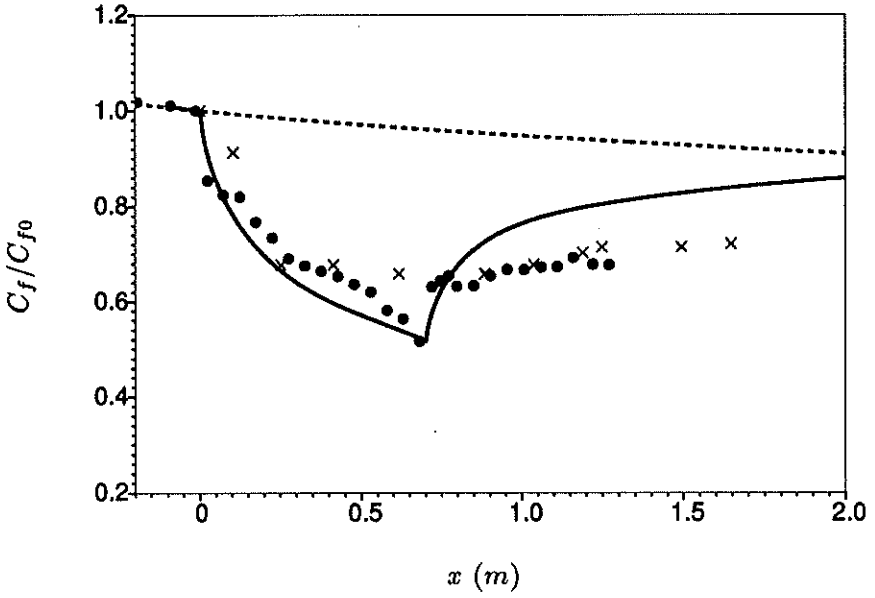

FIGURE 5. Solid line is computed skin friction, normalized on its value at the start of curvature; dashed line is normalized skin friction computed for a flat plate boundary layer. Experimental data on skin friction (×) surface heat flux (•) from Simon *et al.* (1982).

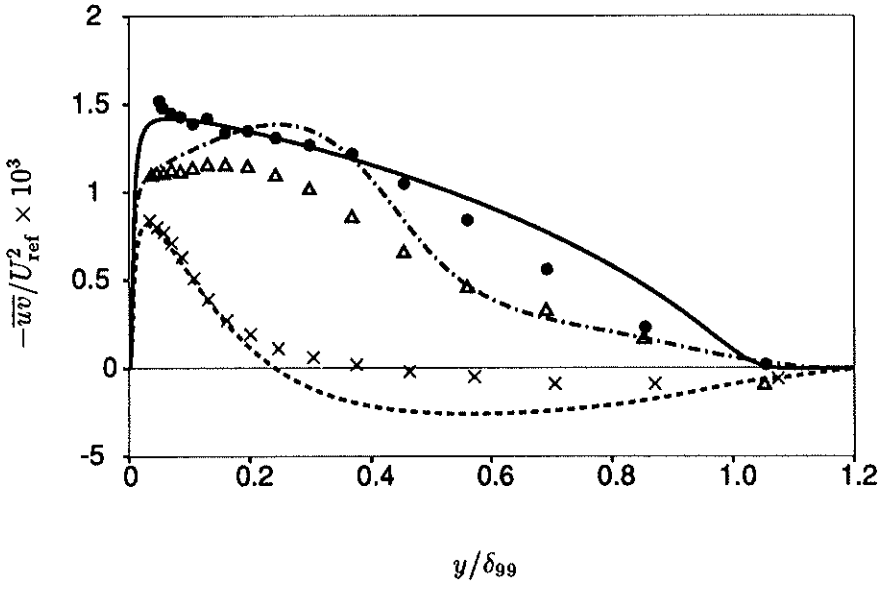

FIGURE 6. Model solutions and experimental data on Reynolds shear stress. The profiles are at $x = -0.062m$ (•, ——), $x = 0.162m$ (×, - - -) and $x = 1.124m$ (△, —·—). These stations are upstream of the bend, 20.6° around the bend and in the downstream recovery region.

stress then propagates across the boundary layer. The model shows some discrepancies with the data. These are most significant in the recovery region downstream of the bend. The model recovers to the flat plate skin friction too rapidly (Figure 5).

2.2 Effects of three-dimensionality

The work described in this section is presented at greater length in Durbin (1992b).

The most clear-cut feature of a three-dimensional boundary layer is the skewing of the direction of the mean velocity vector with height. This may alternatively be described as a presence of mean vorticity in the streamwise direction: in the boundary layer approximation, the vorticity vector is $\mathbf{\Omega} = (\partial_y W, 0, -\partial_y U)$; the projection of the vorticity onto the mean velocity is

$$\mathbf{\Omega} \cdot \mathbf{U} = U^2 \partial_y \left[\frac{W}{U}\right] = U^2 \partial_y \tan(\beta) \tag{11}$$

where β is the direction of the mean velocity relative to the x-axis. In a three-dimensional boundary layer, the quantities in (11) are non-zero; hence, the vorticity and velocity are not orthogonal, and the direction of the mean flow skews with height.

An additional feature of a three-dimensional turbulent shear layer is that the Reynolds stress is not collinear with the mean shear:

$$\frac{\partial_y W}{\partial_y U} \neq \frac{\overline{vw}}{\overline{uv}}$$

or

$$\partial_y U \overline{vw} - \partial_y W \overline{uv} \neq 0. \tag{12}$$

This is the most obvious feature of the turbulence, and has been demonstrated in numerous experiments.

Other effects of three-dimensionality on the turbulence are less clear cut. Many experiments on three-dimensional boundary layers use strong adverse pressure gradients to turn the flow. The role of three dimensionality in this type of experiment is clouded by the presence of the adverse pressure gradient. In order to isolate three- dimensional effects, and to provide comprehensive, accurate data, Moin *et al.* (1990) performed a DNS of pressure driven three-dimensional channel flow. This is a horizontally homogeneous flow produced by subjecting a fully developed two-dimensional channel flow to an accelerating spanwise pressure gradient.

Perhaps the most curious feature of this flow is that the turbulent intensity initially *decreases*. The cross-stream acceleration adds a cross-stream component of mean shear, increasing the magnitude of shear, so one would anticipate an *increase* in the turbulent intensity. Indeed, this flow will ultimately evolve into a two-dimensional channel flow, at an angle to the original flow, with a higher mean velocity and higher turbulent intensity. The initial evolution—which is all that could be numerically simulated—is counter intuitive.

The objective of the present study is to model the behavior of three-dimensional channel flow and then to assess its relevance to the swept wing boundary layer. I considered the possibility that the decrease of the turbulent intensity was due to a suppression of energy redistribution into $\overline{v^2}$, as proposed by Moin *et al.* This was unable to explain the effect. The most direct mechanism, and that which I modeled, is to suppose that the three-dimensionality increases the rate of the energy cascade to small scales.

A parameter is needed to characterize three-dimensionality. This ought to be related to the presence of streamwise vorticity (11) and to the misalignment of stress and shear (12). Consider projection of the production tensor on the direction of the mean vorticity: in a two-dimensional shear layer, $P_{ij}\Omega_i/|\Omega|$ is zero, but not in a three-dimensional layer. This suggests that the invariant $\Omega_i P_{ij}\Omega_j/|\Omega|^2$ might characterize three-dimensionality. Unfortunately, this quantity is identically zero in parallel shear flow. A non-vanishing invariant is $P_{3D}^2 \equiv \Omega_i P_{ij}^2 \Omega_j/|\Omega|^2$, where $P_{ij}^2 = P_{ik}P_{kj}$; this will be used to characterize the effect of three- dimensionality on ε. In parallel shear flow,

$$\Omega_i P_{ij}^2 \Omega_j/|\Omega|^2 = (\partial_y U\overline{vw} - \partial_y W\overline{uv})^2$$

so P_{3D} is related to (12), as required.

The ε-equation both closes the turbulent kinetic energy (k) budget and provides a time-scale for use in modeling: $T = k/\varepsilon$; or in viscous regions, $T = (\nu/\varepsilon)^{1/2}$. The exact equation for ε is of little value to modeling; the usual model equation is based on an *ad hoc* notion that the production and dissipation of ε can be represented by a function of the production and dissipation of energy. Thus, the evolution equation for homogeneous turbulence is assumed to be of the form

$$\dot{\varepsilon} = \frac{\varepsilon}{T} F(P/\varepsilon) \tag{13}$$

where $P = P_{ii}/2$ is the rate of energy production and $F(\bullet)$ is some function. (13) is simply a dimensionally consistent form for expressing the assumed dependence on production and dissipation of energy. The standard ε-equation is obtained by letting $F(\bullet)$ be linear:

$$F(P/\varepsilon) = C_{\varepsilon_1} P/\varepsilon - C_{\varepsilon_2} \tag{14}$$

where the C_ε's are empirical constants. Here we simply extend the argument list to include P_{3D}^2:

$$\dot{\varepsilon} = \frac{\varepsilon}{T} F(P/\varepsilon, P_{3D}^2/\varepsilon^2). \tag{15}$$

Again, we adopt a linear model

$$\dot{\varepsilon} = \frac{C_{\varepsilon_1} P - C_{\varepsilon_2}\varepsilon + C_{\varepsilon_3} P_{3D}^2/\varepsilon}{T}. \tag{16}$$

The value of $C_{\varepsilon 3} = 4$ was chosen.

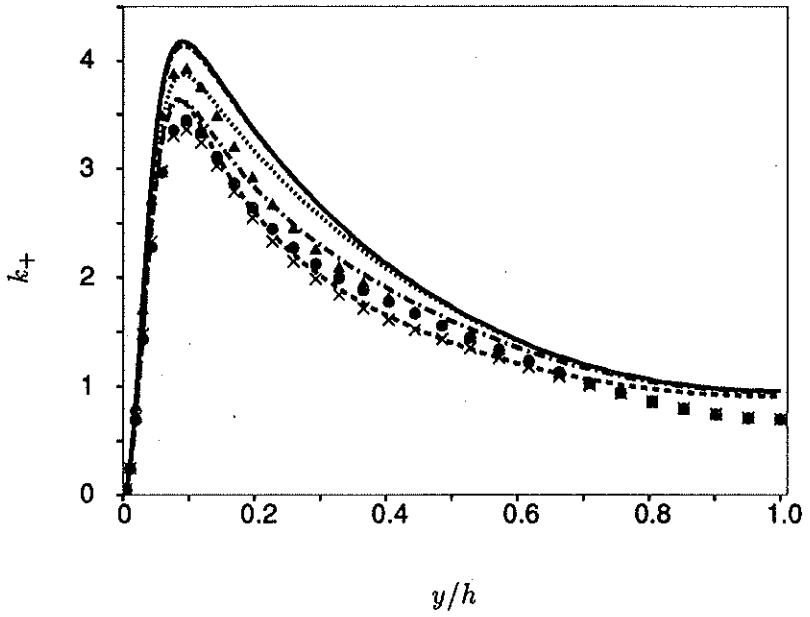

FIGURE 7. Turbulent kinetic energy in 3-D channel flow ($R_\tau = 180$), showing the initial decrease with time. The curves are solutions to the model and symbols DNS data. —— (△), $t = 0$; — - —, $t = 0.3$; ··· (•), $t = 0.6$; — · — (×), $t = 0.9$; - - -, t=1.2.

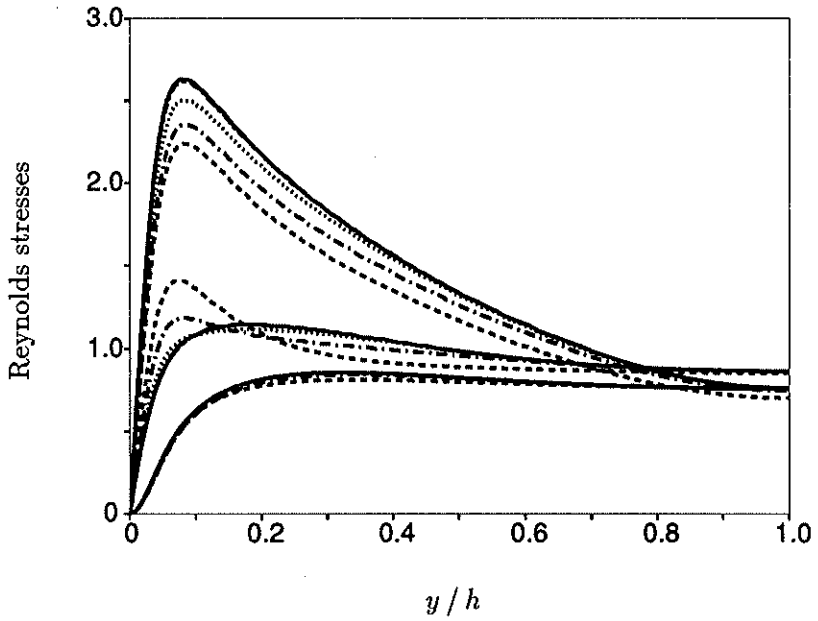

FIGURE 8. Components of turbulent intensity in channel flow. Curves as in Figure 7.

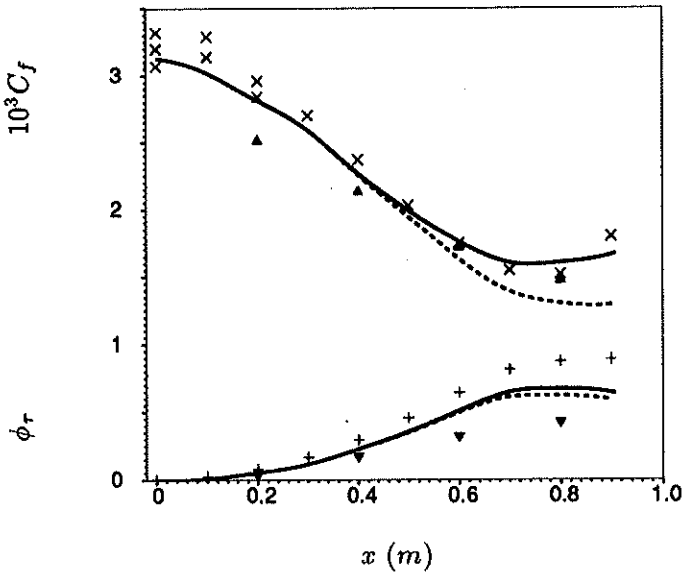

FIGURE 9. Skin friction coefficient and direction of surface stress, in radians, for infinite swept wing boundary layer. Data of Elsenaar and Boelsma (1974): ×, +; data of Pontikos and Bradshaw(1985): △, ▽. Model: ——, $C_{\varepsilon_3} = 4.0$; - - -, $C_{\varepsilon_3} = 0$.

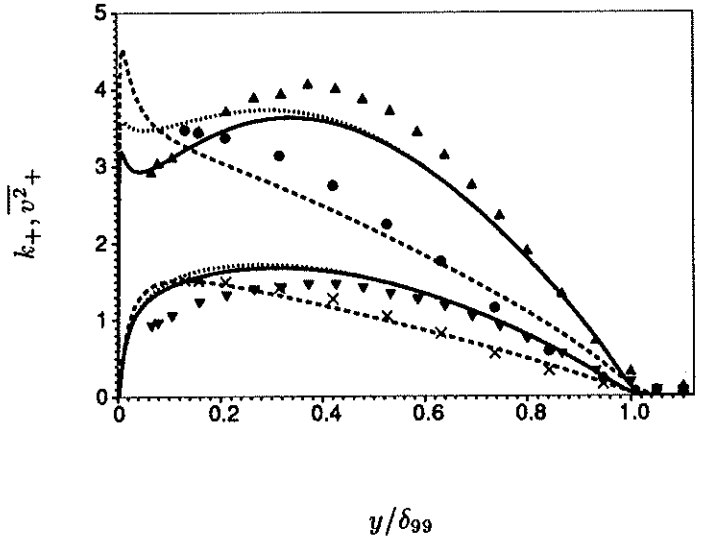

FIGURE 10. Kinetic energy (upper curves) and $\overline{v^2}$ for infinite swept wing; data from Elsenaar and Boelsma (1974). - - - (•, ×), $x = 0.3m$; —— (△, ▽), $x = 0.6m$; · · ·, $x = 0.6m$, $C_{\varepsilon_3} = 0$. Normalization is by friction velocity at $x = 0$ and by 99% boundary layer thickness.

The model described in §2.1 was solved in conjunction with (16). The evolution of the turbulent kinetic energy with time is displayed in Figure 7 along with DNS data. It is seen that the model produces the initial drop of kinetic energy. Figure 8 shows the behavior of individual components of the Reynolds stress tensor. They evolve with time in much the same manner as observed in the Moin *et al.* DNS.

The model was solved for the infinite swept wing flow studied by Elsenaar and Boelsma (1974) and by Bradshaw and Pontikos (1985). This flow was produced by subjecting a boundary layer to a pressure gradient directed at 35° the initial flow direction. The boundary layer originated either at a swept leading edge (Elsenaar and Boelsma) or at a swept suction slot (Bradshaw and Pontikos) so that the whole flow was invariant with respect to translation along lines of constant pressure (ignoring end walls).

The upper curves in Figure 9 show the skin friction coefficient versus downstream distance and the lower curves show the angle of the surface stress to its upstream direction. The solid lines are a solution with $C_{\varepsilon_3} = 4$. The dashed lines are a solution with $C_{\varepsilon_3} = 0$, so that the 3D effect found in the channel flow simulations can be assessed. The two sets of experimental data show how poorly reproducible this experiment is. Given this ambiguity and an ambiguity in the pressure gradient prescribed in the present computation, it cannot be concluded that the three-dimensional effect shown by Figure 9 is significant.

Figure 10 shows profiles of k and $\overline{v^2}$ at two downstream locations. The first is near the beginning of the pressure gradient and the second is well into the three-dimensional region. The sets of curves at $x = 0.6\,m$ show how the model predicts that the 3D effect occurs near to the surface, where it causes a reduction of k. The experimental data suggest that this effect might be present in the flow.

My conclusion is that the three-dimensional effects uncovered in the channel flow DNS have only a minimal influence on the swept wing boundary layer. This is probably because the cross-stream pressure gradient in the DNS was quite large (10 times that of the initial equilibrium flow). In the swept wing experiments the perturbation to the boundary layer was not so abrupt.

3. Future plans

The Reynolds stress model is being solved in increasingly complex flows. The article by S. Ko in this volume describes computations of separated boundary layers. This work on complex flows will continue. A code for computing flow in curvilinear geometries is being developed (with N. Mansour). This will be used to compute turbulent flow on aerofoils.

The possibility of formulating an eddy viscosity transport model for use in complex flows is being explored. Although this is far less satisfactory than Reynolds stress modeling, simple models are preferred by those concerned with complex aerodynamic flows.

REFERENCES

BRADSHAW, P. & PONTIKOS, N. 1985 Measurements in the turbulent boundary

layer on an infinite swept wing. *J. Fluid Mech.* **159,** 105-130.

DURBIN, P. A. 1991 Analyses and modeling of evolving turbulent flow. *CTR Annual Research Briefs.* Stanford Univ./NASA Ames.

DURBIN, P. A. 1992a A Reynolds stress model for near-wall turbulence. *to appear in J. Fluid Mech.*

DURBIN, P. A. 1992b On modeling 3-dimensional wall layers. *CTR manuscript.* **135.**

ELSENAAR, A. & BOELSMA, S.H. 1974 Measurements of the Reynolds stress tensor in a three-dimensional turbulent boundary layer under infinite swept wing conditions. *NLR TR.* **74095 U.**

LAUNDER, B. E. 1989 Second-moment closure: present...and future. *Int. J. Heat and Fluid Flow.* **10,** 282-300.

MOIN, P., SHIH, T. H., DRIVER, D. & MANSOUR, N. 1990 Direct numerical simulation of a three-dimensional turbulent boundary layer. *Phys. Fluids A.* **2,** 1846-1856.

SAMUEL, A. E. & JOUBERT, P. N. 1974 A boundary layer developing in an increasingly adverse pressure gradient. *J. Fluid Mech.* **66,** 481-505.

SIMON, T. W., MOFFATT, R. J., JOHNSTON, J. P. & KAYS, W. M. 1982 Turbulent boundary layer heat transfer experiments: curvature effects including introduction and recovery. *NASA CR.* **3510.**